Roughness effects on the Reynolds stress budgets in near-wall turbulence

Junlin Yuan[1]†, **Ugo Piomelli**[1]

[1]Department of Mechanical and Materials Engineering, Queen's University, Kingston, ON K7L3N6, Canada

The physics of the roughness sublayer are studied by direct numerical simulations of an open-channel flow with sandgrain roughness. A double-averaging approach is used to separate the spatial variations of the time-averaged quantities and the turbulent fluctuations. The spatial inhomogeneity of velocity and Reynolds stresses results in an additional production term for the turbulent kinetic energy, the "wake production"; it is the excess wake kinetic energy, generated from the work of mean flow against the form drag, that is not directly dissipated into heat, but instead converted into turbulence. The wake production promotes wall-normal turbulent fluctuations, and increases the pressure work which ultimately leads to more homogeneous turbulence in the roughness sublayer, and to the increase of Reynolds shear stress and the drag on the rough wall. In the fully rough regime, roughness directly affects the generation of the wall-normal fluctuations, while, in the transitionally rough regime, the region affected by roughness is separated from the region of intense generation of these fluctuations. The budget of the wake kinetic energy and the connection between the wake and the turbulence suggest strong interactions between the roughness sublayer and the outer layer that are insensitive to the variation of the outer-layer conditions. Furthermore, the present results may have implications for the relationship between the roughness geometry and the flow dynamics in the region directly affected by roughness.

Key words: Roughness, turbulence, direct numerical simulation

1. Introduction

Roughness plays an important role in many fields of study. A substantial amount of work has been carried out to understand the dynamics of turbulent flows over rough walls, both for engineering and atmospheric applications. Roughness effects on the flow are summarised by Raupach *et al.* (1991) and Jiménez (2004). Roughness increases the drag on the wall due to the pressure drag, resulted from the wake created downstream of a roughness element. Many studies have shown that, far away from the wall, roughness does not affect the turbulent statistics, but it sets the velocity scale by increasing the friction coefficient.

Inside the roughness sublayer (defined as the region where roughness causes spatial variations of time-averaged turbulent statistics), the flow dynamics are significantly altered as the turbulent structures become more three-dimensional. In order to capture the interaction between the turbulence and the spatial variation of the time-averaged velocity field (wake), the space-time double-averaging approach can be used (Raupach & Shaw

† Email address for correspondence: junlin.yuan@queensu.ca

1982). Earlier studies of the flow over canopies (Finnigan 2000; Raupach *et al.* 1991) found that the wake leads to an additional source term in the budget of the turbulent kinetic energy (TKE), the "wake production".

Roughness and sediments are different from canopies in the vertical distribution of the density of the roughness elements. Recent studies on flow over gravel beds (Mignot *et al.* 2009; Dey & Das 2012) found that the effect of the wake on TKE is negligible compared to the production due to the shear of the mean velocity (shear production).

Direct and large-eddy simulations have studied the roughness effects on wall-bounded flows, *e.g.*, Kanda *et al.* (2004), Coceal *et al.* (2006), Orlandi & Leonardi (2008), Leonardi & Castro (2010), and Lee *et al.* (2011). Their main focus has been on the flow above the roughness and the parameterization of the drag. The layer below the roughness crest, howeve, is also important; understanding this layer would provide insights to the roughness effects in the regions above. It was observed by Coceal *et al.* (2006) that the wake depends on the geometry of the roughness, and that, although smaller than the Reynolds stresses, the dispersive stresses (resulting from the wake component) are significant in the lower part of the roughness sublayer. However, the effects of roughness on the budgets of specific Reynolds normal stresses are not well studied. It is important to understand the roughness effects on the wall-normal and spanwise turbulent fluctuations, since these two components are more direct indicators (than TKE) of inner-outer-layer interactions, near-wall structure instability, and drag generation. To this end, we use direct numerical simulations of the turbulent flow over sandgrain roughness in the transitionally and fully rough regimes, to study the roughness effects on the budgets of the Reynolds stresses, and to investigate the energy transfer between the wake and the turbulence.

2. Problem formulation

2.1. *Governing equations and numerical techniques*

The incompressible flow of a Newtonian fluid is governed by the equations of conservation of mass and momentum,

$$\frac{\partial u_i}{\partial x_i} = 0, \tag{2.1}$$

$$\frac{\partial u_i}{\partial t} + \frac{\partial u_i u_j}{\partial x_j} = -\frac{\partial P}{\partial x_i} + \nu \frac{\partial^2 u_i}{\partial {x_j}^2} + F_i, \tag{2.2}$$

where u_i and P are the velocities and pressure.

x_1, x_2 and x_3 (or x, y and z) are, respectively, the streamwise, wall-normal and spanwise directions, and u_i (or u, v and w) are the velocity components in those directions; $P = p/\rho$ is the modified pressure, ρ the density and ν the kinematic viscosity. We performed direct numerical simulations of (2.1) and (2.2) using a staggered grid and second-order, central differences for all terms, a second-order semi-implicit time advancement, and MPI (Message Passing Interface) parallelization (Keating *et al.* 2004). An immersed-boundary method (IBM) based on the volume-of-fluid approach (Scotti 2006; Yuan & Piomelli 2014) is applied: a body force, F_i is used to impose the no-slip boundary condition on the rough surfaces; it is non-zero in the interface cell only. Details on the model can be found in Yuan & Piomelli (2014).

2.2. *Averaging approach*

Following Mignot *et al.* (2009), a double-averaging (DA) approach is applied to decompose a flow quantity, θ, into space-time average, $\langle\overline{(\cdot)}\rangle$ (bar and brackets denote temporal

and spatial averages, respectively), the spatial disturbance of the temporal average, $\widetilde{(\cdot)}$, and the turbulent fluctuation (denoted by the prime),

$$\theta(x,y,z,t) = \langle\overline{\theta}\rangle(y) + \widetilde{\theta}(x,y,z) + \theta'(x,y,z,t). \tag{2.3}$$

Two spatial averaging approaches are used (Nikora *et al.* 2007). The intrinsic spatial average, $\langle\cdot\rangle$, is carried out in the (x,z)-plane, in the fluid domain only, while the superficial average, $\langle\cdot\rangle_s$, is carried out over the whole (x,z)-plane.

Applying the intrinsic average to the time-averaged u-momentum equation for the open-channel flow, one obtains

$$-\left\langle\frac{\partial\overline{P}}{\partial x}\right\rangle + \nu\left\langle\nabla^2\overline{u}\right\rangle - \left\langle\frac{\partial\overline{u}\,\overline{v}}{\partial y}\right\rangle - \left\langle\frac{\partial\overline{u'v'}}{\partial y}\right\rangle = 0. \tag{2.4}$$

Note that the IBM force F_i does not appear in (2.4) since it is zero inside the fluid domain. Equation (2.4) can be written as

$$-\frac{\partial\langle\overline{P}\rangle_s}{\partial x} + \nu\frac{\partial^2\langle\overline{u}\rangle_s}{\partial y^2} - \frac{\partial\langle\overline{u'v'}\rangle_s}{\partial y} - \frac{\partial\langle\widetilde{u}\,\widetilde{v}\rangle_s}{\partial y} - \left\langle\frac{\partial\widetilde{P}}{\partial x}\right\rangle_s + \nu\langle\nabla^2\widetilde{u}\rangle_s = 0, \tag{2.5}$$

where the last two terms on the left hand side are, respectively, the pressure drag, f_p, and the viscous drags, f_ν (Raupach & Shaw 1982); they arise due to the non-commutativity between the operators $\partial/\partial x_i$ and $\langle\cdot\rangle$ below the roughness crest. The sum of these two terms is the total drag. It can be shown that F_1, averaged in the interface cell in the (x,z)-plane, equals the total drag, $-\langle\partial\widetilde{P}/\partial x\rangle_s + \nu\langle\nabla^2\widetilde{u}\rangle_s$.

2.3. *Simulation parameters*

An open-channel flow of domain size $6h \times 1h \times 3h$ in x, y, and z is simulated; this size is sufficient to accommodate the largest turbulent structures on a smooth-wall channel flow. No-slip and symmetric boundary conditions are applied to the bottom wall and to the top boundary, respectively. Periodic conditions are used in both the x- and z-directions. A constant pressure gradient is applied to drive the flow. A virtual sandgrain model (Scotti 2006) is used to impose roughness at the bottom boundary: the bottom domain is separated into tiles of size around $2k_s \times 2k_s$; in each tile a roughness element is planted, which constitutes a randomly rotated ellipsoid with semiaxes equaling k_s, $1.4k_s$, and $2k_s$. Note that, for this virtual sandgrain surface, k_s is known *a priori* since the model is calibrated, in a specific range of roughness Reynolds numbers, to give the same roughness function as the Nikuradse sandgrain with a height k_s; however, the shape of the elements is not exactly the same as those of Nikuradse. A fraction of the surface is visualized in Figure 1(a) as iso-surface of the fluid volume fraction equaling 0.5. The Reynolds number based on the half-channel height (h) and the friction velocity (u_τ) is $Re_\tau = 1000$. Two roughness heights are used to yield a transitionally rough and a fully rough flow: a low-roughness case (R1, $k_s/h = 0.02$, $k_s^+ = 22$), and a high-roughness one (R2, $k_s/h = 0.07$, $k_s^+ = 72$). The roughness crests (k_c) for R1 and R2 are 3% and 9% of h, respectively. A smooth-wall case (case SM) is also included for comparison.

Table 1 tabulates the parameters and spatial resolutions. Uniform grids are used in x and z, while the grid is refined near the wall in y direction. For the rough cases, $\Delta y^+ < 1$ for $y \leqslant k_c$, resulting in more than 31 and 51 grid points in y below the mean roughness height and the crest, respectively. For the smooth case, $\Delta y^+_{\min} = 0.3$, with 4 points below $y^+ = 1$. The total number of grid points varies between 70 and 130 millions. The grid sizes in x and z directions are less than or equal to 12 and 6 wall units, respectively, sufficient for DNS resolution.

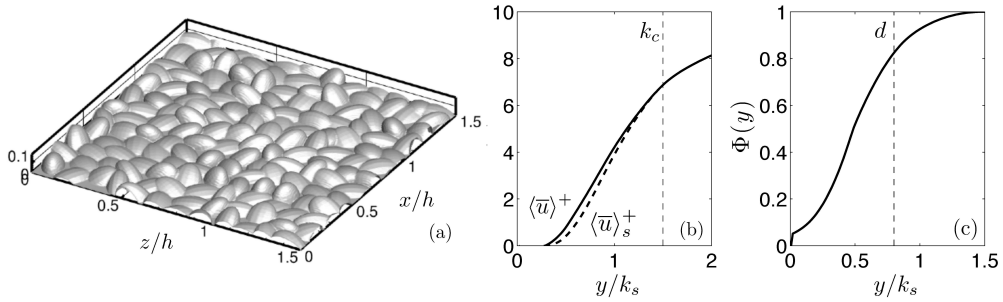

FIGURE 1. (a) Visualization of 1/8 of the surface R2; wall-normal profiles of (b) DA streamwise velocity (——— $\langle\overline{u}\rangle$ and - - - $\langle\overline{u}\rangle_s$) and (c) roughness geometry function.

Case	k_s^+	k_s/h	k_c/h	$\overline{k}/h$	$N_x \times N_z$	$n_i \times n_k$	$\Delta x^+ \times \Delta z^+$
SM	0	0	0	0	–	512×512	12×6
R1	22	0.02	0.03	0.013	7×7	1024×512	6×6
R2	72	0.07	0.09	0.040	20×20	1024×512	6×6

TABLE 1. Parameters for all cases. k_c: roughness crest; $\overline{k}$: mean roughness height. n_j ranges from 128 to 256. N_{x_i}: grid points per sand-grain element.

The shape resolution of a roughness element is quantified by N_{x_i}, the number of grid points (in x_i) used to resolve the shape of each sandgrain element. A grid-convergence study (not shown) was carried out, and it was found that the present resolution is sufficient to obtain the Reynolds stresses and their budgets. For all cases, data are collected from a total simulation time of $T = 50h/u_\tau$ after the transient. A convergence study showed that decreasing the simulation time to $0.5T$ leads to errors of less than 1% for third- or lower order turbulent statistics.

3. Results

3.1. *Turbulent statistics*

The DA streamwise velocity is shown in Figure 1(b). Below the roughness crest, the velocity varies almost linearly, consistent with Model III of the velocity distribution proposed by Nikora *et al.* (2004) applied to rough-wall flows with relatively low submergence (h/k_s). The superficial average ($\langle\overline{u}\rangle_s = \Phi\langle\overline{u}\rangle$) is lower than the intrinsic one, since the roughness geometry function, $\Phi(y)$, defined as the fraction of space occupied by fluid in the horizontal plane at y, is less than one (Figure 1(c)). The distribution of $\Phi(y)$ is not affected by the variation of the spatial resolution. The zero-plane displacement (d), representing the effective elevation of the boundary layer due to roughness, is obtained as the location of the centroid of the wall-normal averaged drag-force profile (Yuan & Piomelli 2014); $d \approx 0.8k_s$ for both rough cases.

Figure 2(a) shows the DA velocity profiles in wall units. The roughness functions, ΔU^+, obtained as the offsets of $\langle\overline{u}\rangle_s^+$ profiles in the logarithmic region from the universal logarithmic law, are 3.5 and 7.8 for cases R1 and R2, respectively, yielding $k_s^+ = 22$ and 72 based on the Colebrook correlation (Colebrook 1939); case R2 is in the fully rough regime, while case R1 is transitionally rough.

The Reynolds stresses in cases R1 and R2 are compared in Figure 2(b) with smooth-

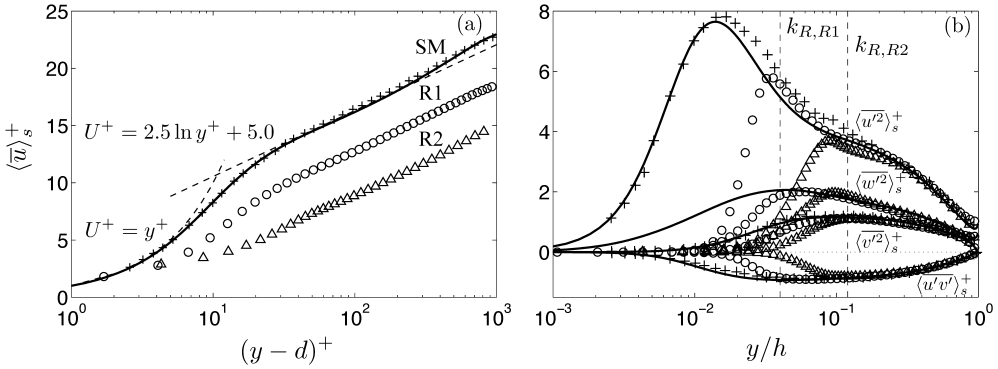

FIGURE 2. (a) Streamwise velocity and (b) Reynolds stresses for cases SM (——), R1 (○), and R2 (△). + smooth-wall experiment (Schultz & Flack 2013). k_R: top of the roughness sublayer.

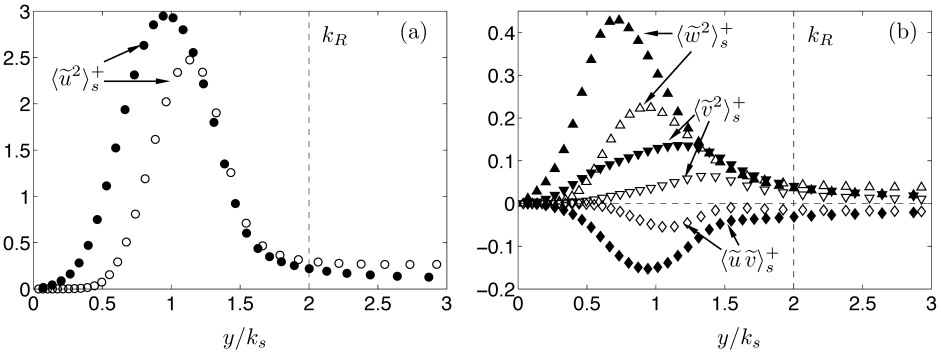

FIGURE 3. Form-induced stresses for cases R1 (empty symbols) and R2 (filled symbols): (a) $\langle \widetilde{u}^2 \rangle_s^+$, (b) ▽ $\langle \widetilde{v}^2 \rangle_s^+$, △ $\langle \widetilde{w}^2 \rangle_s^+$, and ◇ $\langle \widetilde{u}\,\widetilde{v} \rangle_s^+$.

wall experimental data from channel-flow studies with the same Reynolds number (Schultz & Flack 2013); agreement is obtained in the outer layer, supporting the wall similarity hypothesis. Case R1 preserves a high near-wall peak of the streamwise normal Reynolds stress, while the peak is significantly damped for case R2, due to the destruction of the buffer layer. The top of the roughness sublayer is denoted by k_R; its location will be discussed below. Inside the roughness sublayer, all normal Reynolds stresses in wall units are damped, compared to case SM. The magnitudes of the other two shear stresses are negligible compared to $\langle \overline{u'v'} \rangle$, due to the randomness of the rough surface.

The form-induced (or dispersive) stresses are shown in Figure 3 for both rough cases; the wall-normal and spanwise components are smaller than the corresponding components of the Reynolds stresses, consistent with previous experimental rough-wall and canopy studies (Nikora *et al.* 2001; Mignot *et al.* 2009); the streamwise form-induced stress is comparable to the Reynolds stress, a characteristic of relatively low submergence (Manes *et al.* 2007). The peak of $|\langle \widetilde{u}\,\widetilde{v} \rangle_s^+|$ is around 0.15, consistent with previous DNS study by Coceal *et al.* (2006). The region with non-negligible $\langle \widetilde{u}_i^2 \rangle_s$ is the roughness sublayer, whose thickness, k_R, is shown to be around $2k_s$. The magnitude of the form-induced stresses relative to the Reynolds stresses increases with k_s^+, since, in the roughness sublayer, $\langle \overline{u_i'^2} \rangle^+$ decreases while $\langle \widetilde{u}_i^2 \rangle^+$ increases with higher k_s^+, due to the lower submergence.

Figure 4 shows the stress balance for case R2; the mean pressure gradient is balanced

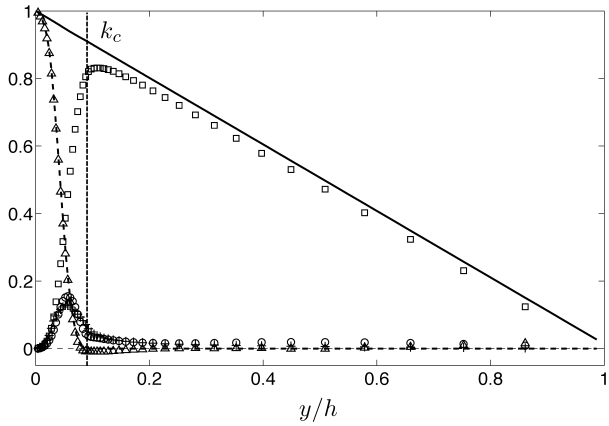

FIGURE 4. Stress balance of case R2. ——— Total stress from momentum balance, △ total drag from momentum balance, - - - total drag from F_1 integral, □ Reynolds shear stress, ○ form-induced shear stress, + viscous stress due to mean shear.

by the sum of other stresses,

$$\tau^+ = \int_{y^+}^{h^+} (f_\nu^+ + f_p^+) dy^+ - \langle \overline{u'v'} \rangle_s^+ + \frac{\partial \langle \overline{u} \rangle_s^+}{\partial y^+} - \langle \widetilde{u}\,\widetilde{v} \rangle_s^+ = 1 - \frac{y^+}{h^+}. \tag{3.1}$$

The viscous stress is small, consistent with fully rough flow. The form-induced shear stress is also small compared to the Reynolds shear stress. The total drag, $(f_\nu^+ + f_p^+)$, calculated from momentum balance, agrees with the IBM force, $\langle F_1 \rangle_s$, which can be used to calculate the total drag, as shown by Yuan & Piomelli (2014).

3.2. *Budgets of Reynolds and dispersive stresses*

In the turbulent flow over roughness, the total kinetic energy can be decomposed into three parts,

$$\frac{1}{2}\langle \overline{u_i u_i} \rangle = \frac{1}{2}\langle \overline{u}_i \rangle \langle \overline{u}_i \rangle + \frac{1}{2}\langle \widetilde{u}_i \widetilde{u}_i \rangle + \frac{1}{2}\langle \overline{u_i' u_i'} \rangle, \tag{3.2}$$

where the terms on the right hand side are, respectively, the mean-flow kinetic energy (MKE), the wake kinetic energy (WKE) and the TKE. The MKE is converted to small-scale TKE (and consequently heat) in two ways (Finnigan 2000): first, the energy goes through the whole energy cascade; second, MKE first generates WKE of scale k_s due to the work of the mean flow against the total drag, and the WKE generates TKE of scales smaller than k_s through the energy cascade ("short-circuited" cascade (Raupach *et al.* 1991)). The interactions between WKE and TKE are also two-ways: WKE generates TKE of scales smaller than k_s, while TKE is converted to WKE through the work of large-scale turbulent structures against the form drag.

The budget of Reynolds stresses and TKE were derived by Raupach & Shaw (1982) for flow over canopy and by Mignot *et al.* (2009) for flow over roughness. The budgets of the normal Reynolds stresses are (no summation over Greek index)

$$-2\langle \overline{u_\alpha' v'} \rangle \frac{\partial \langle \overline{u}_\alpha \rangle_s}{\partial y} - 2\left\langle \widetilde{u_\alpha' u_j'} \frac{\partial \widetilde{u}_\alpha}{\partial x_j} \right\rangle_s - \frac{\partial}{\partial y}\langle \widetilde{u_\alpha' u_\alpha'} \widetilde{v} \rangle_s - \frac{\partial}{\partial y}\langle \overline{u_\alpha' u_\alpha' v'} \rangle_s$$
$$-2\left\langle \overline{u_\alpha' \frac{\partial P'}{\partial x_\alpha}} \right\rangle_s + \nu \frac{\partial^2}{\partial y^2}\langle \overline{u_\alpha' u_\alpha'} \rangle_s - \epsilon_{\alpha\alpha} = 0. \tag{3.3}$$

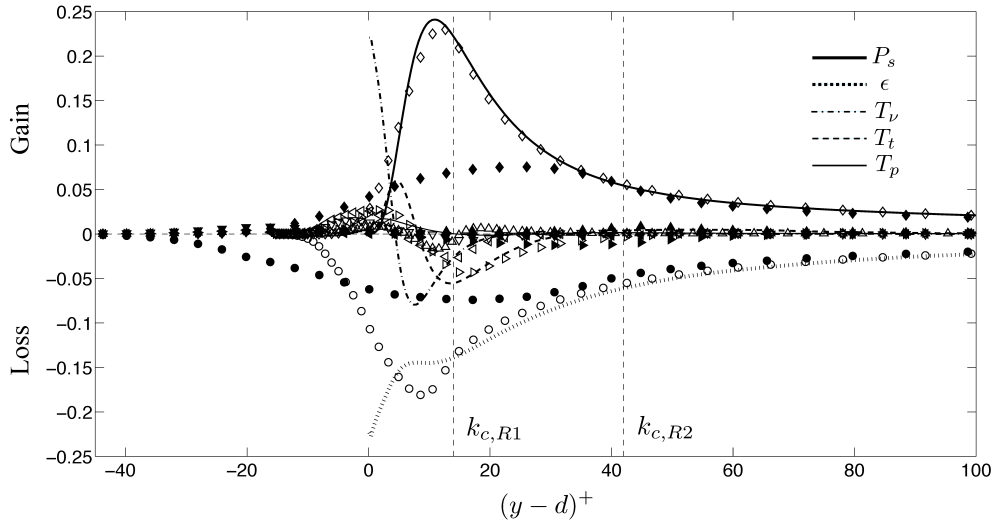

FIGURE 5. TKE budgets for cases SM (line), R1 (empty symbol), and R2 (filled symbol). All terms normalized by u_τ^4/ν. **- - -** k_c, roughness crest. $\diamond$ P_s, $\triangle$ P_w, $\circ$ ϵ, $\triangleright$ T_t, $\triangleleft$ T_ν, $\triangledown$ T_p. Note that the actual bottom-wall location varies.

Summing over the three components yields the budget of the TKE,

$$-\langle\overline{u_i'v'}\rangle\frac{\partial\langle\overline{u}_i\rangle_s}{\partial y}-\left\langle\widetilde{u_i'u_j'}\frac{\partial\widetilde{u}_i}{\partial x_j}\right\rangle_s-\frac{\partial}{\partial y}\langle\widetilde{u_i'u_i'}\widetilde{v}\rangle_s/2$$
$$-\frac{\partial}{\partial y}\langle\overline{u_i'u_i'v'}\rangle_s/2-\frac{\partial}{\partial y}\langle\overline{P'v'}\rangle_s+\nu\frac{\partial^2}{\partial y^2}\langle\overline{u_i'u_i'}/2\rangle_s-\epsilon_k=0, \tag{3.4}$$

where the terms on the left hand side are, respectively, shear production (P_s), wake production (P_w), transport due to wake, turbulent transport (T_t), pressure transport (T_p), viscous transport (T_ν), and viscous dissipation (ϵ). ϵ is obtained as the residual of the sum of all other terms. In the normal-stress budget the pressure work, $\Pi_{\alpha\alpha}$, is also present.

The budget of WKE, $1/2\langle\widetilde{u}_i\widetilde{u}_i\rangle$, was derived by Raupach & Shaw (1982). Taking into account the vertically varying roughness geometry function, $\Phi(y)$, the budgets of the normal dispersive stresses ($\langle\widetilde{u}_\alpha^2\rangle$) read

$$-2\langle\widetilde{u}_\alpha\widetilde{v}\rangle\frac{\partial\langle\overline{u}_\alpha\rangle_s}{\partial y}+2\left\langle\widetilde{u_\alpha'u_j'}\frac{\partial\widetilde{u}_\alpha}{\partial x_j}\right\rangle_s-\frac{\partial}{\partial y}\langle\widetilde{u}_\alpha\widetilde{u}_\alpha\widetilde{v}\rangle_s-2\frac{\partial}{\partial y}\langle\widetilde{u}_\alpha\widetilde{u_\alpha'v'}\rangle_s$$
$$-2\left\langle\widetilde{u}_\alpha\frac{\partial\widetilde{P}}{\partial x_\alpha}\right\rangle_s+2\nu\langle\widetilde{u}_\alpha\nabla^2\widetilde{u}_\alpha\rangle_s=0 \tag{3.5}$$

where the six terms on the left hand side are, respectively, shear production of WKE, wake production ($-P_w$), transport due to wake, transport due to turbulence, work done by pressure, and viscous diffusion and dissipation at the wake level.

The term P_w appears with opposite signs in the budgets of TKE and WKE; it is the net transfer from WKE to TKE as the result of their interactions. Previous studies on flows above canopies found that P_w is usually positive (WKE converts to TKE) with magnitudes comparable to P_s (Raupach *et al.* 1991; López & García 2001). In the experimental study of flow over gravel beds (Mignot *et al.* 2009), however, the magnitude of P_w was found to be less than 5% of P_s.

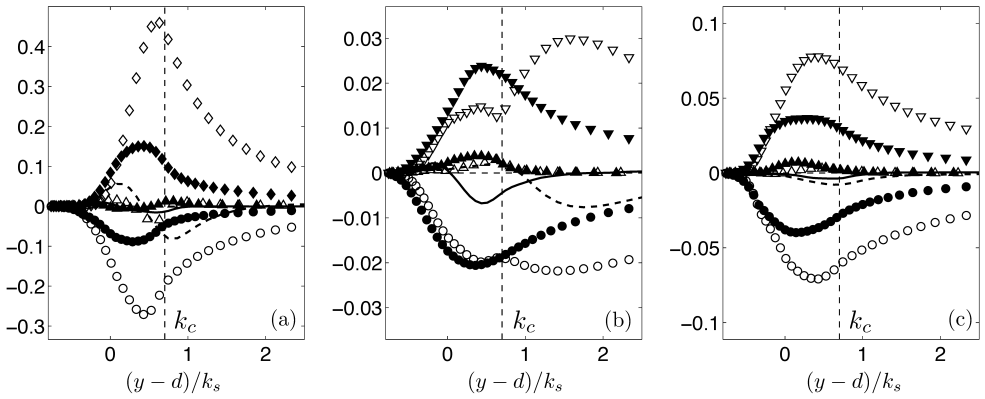

FIGURE 6. Comparison of normal Reynolds stress budgets between cases R1 (empty symbols) and R2 (filled symbols): (a) streamwise, (b) wall-normal, and (c) spanwise components. $\diamond$ P_s, $\triangle$ P_w, $\circ$ ϵ, and $\triangledown$ Π; - - - T_t for case R1, ——— T_t for case R2 . All terms normalized by u_τ^4/ν.

The TKE budgets normalized by wall units are shown in Figure 5. Case SM has been validated with the smooth-wall channel-flow DNS results reported by Hoyas & Jiménez (2008) (not shown). Above the roughness sublayer ($y > k_R$), the R1 budget terms agree well with case SM, but in the roughness sublayer, they differ from the smooth case mainly in that, approaching the wall, both ϵ_k and T_ν become zero, indicating a quiet region without turbulence at the root of the roughness.

Figure 5 also shows that, for both rough cases, the location of the peak of the shear production is close to the roughness crest, connected to the shear layers formed near the crest (Mignot *et al.* 2009; Ikeda & Durbin 2007). For case R2, P_s peaks at $0.73k_c$ from the actual bottom wall (where $\Phi = 0$), while, for case R1, it peaks at $0.93k_c$. It was observed by Mignot *et al.* (2009) that, for flow over gravel beds, P_s peaks around $0.9k_c$. P_s decreases from its peak location to the virtual wall. Dissipation peaks slightly below the production peak; the transport terms are non-negligible in the roughness sublayer only. Both the turbulent diffusion and the viscous diffusion take energy from the region with high production (near k_c) and transport it towards the wall to balance dissipation. These observations are consistent with the literature (Finnigan 2000; Mignot *et al.* 2009; Hong *et al.* 2011). Furthermore, the pressure transport removes TKE from near the roughness crest, and transports it to the lower part of the roughness sublayer; for case R2, the pressure transport is the most important source term in the lowest third of the sublayer, consistent with LES results in flow within forest canopy (Dwyer *et al.* 1997), while in the transitionally rough case R1, the viscous diffusion is the most important source term in the lowest part of the sublayer. Compared to P_s and ϵ, P_w is much smaller, consistent with Mignot *et al.* (2009). The sign and magnitude of P_w are affected by the roughness height, which will be explained later.

Selected terms of the normal Reynolds stress budgets (in wall units) are shown in Figure 6. The wall-normal distance is normalized using k_s. As the flow approaches the fully rough regime from R1 to R2, $P^+_{s,uu}$ decreases significantly; so do the viscous dissipations of $\langle\overline{u'^2}\rangle$ and $\langle\overline{w'^2}\rangle$, while, below the roughness crest, Π^+_{vv} increases. This indicates that roughness results in more energy being redistributed to $\langle\overline{v'^2}\rangle$, and that stronger wall-normal fluctuations distort the near-wall quasi-streamwise vortices, homogenizing the turbulence near the wall, consistent with the previous observations from DNS that roughness disturbs the near-wall low-speed streaks (Lee *et al.* 2011).

For case R1, Π^+_{vv} exhibits two peaks; the inner peak is located slightly below the

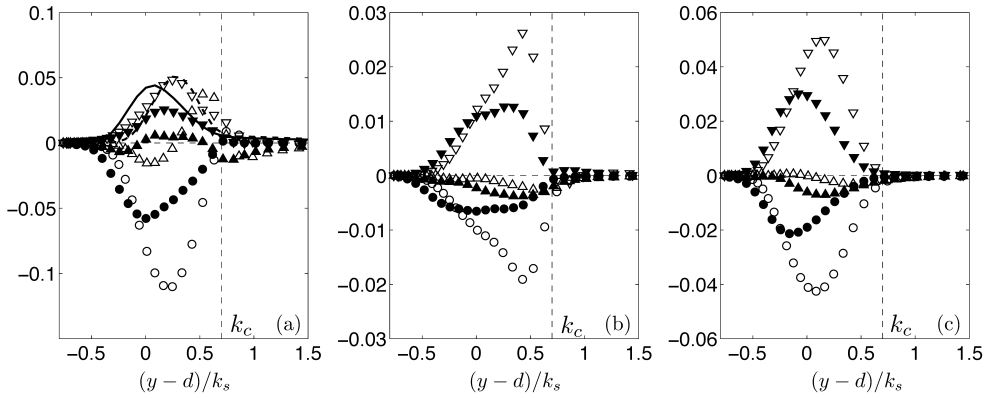

FIGURE 7. Comparison of normal form-induced stress budgets between cases R1 (empty symbols) and R2 (filled symbols): (a) streamwise, (b) wall-normal, and (c) spanwise components. Line: shear production (- - - R1, ——— R2), ▽ pressure work, △ $-P_w$, and ○ viscous dissipation and diffusion. All terms normalized by u_τ^4/ν.

roughness crest, where the shear production peaks, while the outer peak is outside the roughness sublayer, at $(y-d)^+ \approx 30$. The outer peak exceeds dissipation, with the excess energy transported into the region of the inner peak. As the roughness height increases from R1 to R2, the inner peak of Π_{vv}^+ moves upwards and merges into the outer peak. Meanwhile, excess energy is gained around the roughness crest, and transported both towards the wall and towards the outer layer. This indicates that, in a transitionally rough flow, the roughness is somewhat isolated from the most important region for the generation of wall-normal turbulent fluctuations, while, in a fully rough flow, roughness directly affects its generation.

The wake production for $\langle\overline{u'^2}\rangle$ is mostly negative below k_c for R1 and and negligible for R2; for the other two normal components, it is positive, with non-negligible peak magnitudes compared to the pressure work ($17\%\Pi_{vv}$ and $23\%\Pi_{ww}$ in case R2). Such difference may be due to the fact that $\langle\overline{u'^2}\rangle$ is mostly associated with turbulent structures with larger scale than the roughness length scale, converting significant amount of TKE to WKE as they work against the form drag; therefore, more $\langle\overline{u'^2}\rangle$ is converted to WKE compared to the amount being converted from WKE, hence the negative $P_{w,uu}$. On the other hand, $\langle\overline{v'^2}\rangle$ and $\langle\overline{w'^2}\rangle$ receive a more significant contribution from turbulent structures smaller than k_s; thus $\langle\overline{v'^2}\rangle$ and $\langle\overline{w'^2}\rangle$ generate less WKE than the amount being converted from WKE through energy cascade. For v' and w' intensities, the wake production is important, despite a weaker wake contribution to the TKE budget.

Figure 7 shows the dispersive stress budgets. Two significant sources are present: the shear production and the pressure work. The shear production is due to the work of the mean flow against the form-induced stress; it contributes to $\langle\widetilde{u}^2\rangle$ only. The pressure work of WKE can be written as

$$\left\langle \widetilde{u}_i \frac{\partial \widetilde{P}}{\partial x_i} \right\rangle_s = -\frac{\partial \langle \widetilde{P}\widetilde{v}\rangle_s}{\partial y} + \langle\overline{u}\rangle_s \left\langle \frac{\partial \widetilde{P}}{\partial x} \right\rangle, \tag{3.6}$$

with the two terms on the right hand side being the pressure transport and the energy gained from the mean flow working against the form drag; the latter is shown contributing significantly to $\langle\widetilde{u}^2\rangle$ and is the only source of $\langle\widetilde{v}^2\rangle$ and $\langle\widetilde{w}^2\rangle$. The WKE is partly converted to TKE through wake production, partly dissipated into heat. As the roughness height increases from R1 to R2, a larger portion of $\langle\widetilde{v}^2\rangle$ and $\langle\widetilde{w}^2\rangle$ is converted to Reynolds

stresses instead of being directly dissipated, due to the further separation between the roughness length scale and the viscous length scale.

Conclusions

Direct numerical simulations are carried out in open-channel flows over sand-grain roughness in the transitionally and the fully rough regimes. A double-averaging (DA) technique is applied to separate the spatial disturbance of the time-averaged field and the turbulent field. Significant spatial variations of time-averaged flow quantities are generated due to the three-dimensionality of the roughness geometry. The form-induced stresses are small compared to their Reynolds stress counterparts, but the magnitude of this difference becomes smaller as the roughness height increases.

The work of the form drag near k_c converts mean-flow energy to wake energy, which is partly dissipated into heat and partly converted to turbulence through wake production. The intensified wall-normal turbulent fluctuations lead to higher pressure work near k_c, and more homogeneous energy redistribution between the Reynolds stresses. In the fully rough regime, the wake dynamically affects the region of $\langle\overline{v'^2}\rangle$ generation, while, in the transitionally rough regime, its effect is limited below k_c.

Despite significant transfer from the wake to the turbulent component in the wall-normal and spanwise directions, for the streamwise component, the conversion is mostly from turbulence to wake energy, further contributing to a more even TKE redistribution; this is possibly due to the larger turbulent scales that are associated with this Reynolds stress component. The wake production of TKE, however, is negligible, because its values for the three normal Reynolds stresses tend to cancel out, and the magnitudes of total TKE production and dissipation are greater than the energy redistributed.

The current results shed some light on the role of the spatial inhomogeneity on the generation of drag in rough-wall boundary layers. The spatial inhomogeneity, being dependent on the roughness geometry, and in turn altering the energy redistribution and strongly affecting the Reynolds shear stress through its production, may provide the link between geometry detail and the dynamics in the roughness sublayer. Furthermore, the fact that the wake energy depends on the work of mean flow against the form drag as a source term suggests that the wake field is more persistent compared to turbulence in a non-equilibrium boundary layer: while the turbulence production relies on active fluctuations and the mean shear, the presence of the wake requires non-zero mean velocity only. The persistent wake indicates strong interactions between the roughness sublayer and the outer layer, insensitive to the variation of the outer-layer conditions.

Support from Hydro Québec, the Natural Science and Engineering Research Council of Canada (NSERC), and the High Performance Computing Virtual Laboratory (HPCVL) is acknowledged.

REFERENCES

Coceal, O., Thomas, T. G., Castro, I. P. & Belcher, S. E. 2006 Mean flow and turbulence statistics over groups of urban-like cubical obstacles. *Bound.-Lay. Meteorol.* **121**, 491–519.

Colebrook, C. F. 1939 Turbulent flow in pipes with particular reference to the transition region between smooth- and rough-pipe laws. *J. Inst. Civ. Eng.* **11**, 133–156.

Dey, S. & Das, R. 2012 Gravel-bed hydrodynamics: double-averaging approach. *J. Hydr. Engng* **138**, 707–725.

Dwyer, M. J., Patton, E. G. & Shaw, R. H. 1997 Turbulent kinetic energy budgets from a

large-eddy simulation of airflow above and within a forest canopy. *Bound.-Lay. Meteorol.* **84**, 23–42.

Finnigan, J. 2000 Turbulence in plant canopies. *Annu. Rev. Fluid Mech.* **32**, 519–571.

Hong, J., Katz, J. & Schultz, M. P. 2011 Near-wall turbulence statistics and flow structures over three-dimensional roughness in a turbulent channel flow. *J. Fluid Mech.* **667**, 1–37.

Hoyas, S. & Jiménez, J. 2008 Reynolds number effects on the Reynolds-stress budgets in turbulent channels. *Phys. Fluids* **20**, 101511–1–9.

Ikeda, T. & Durbin, P. A. 2007 Direct simulations of a rough-wall channel flow. *J. Fluid Mech.* **571**, 235–263.

Jiménez, J. 2004 Turbulent flows over rough walls. *Annu. Rev. Fluid Mech.* **36**, 173–196.

Kanda, M., Moriwaki, R. & Kasamatsu, F. 2004 Large-eddy simulation of turbulent organized structures within and above explicitly resolved cube arrays. *Bound.-Lay. Meteorol.* **112**, 343–368.

Keating, A., Piomelli, U., Bremhorst, K. & Nešić, S. 2004 Large-eddy simulation of heat transfer downstream of a backward-facing step. *J. Turbul.* **5**, 20–1—27.

Lee, J. H., Sung, H. J. & Krogstad, P.-Å 2011 Direct numerical simulation of the turbulent boundary layer over a cube-roughened wall. *J. Fluid Mech.* **669**, 397–431.

Leonardi, S., S. & Castro, I. P. 2010 Channel flow over large cube roughness: a direct numerical simulation study. *J. Fluid Mech.* **651**, 519–539.

López, F. & García, M. H. 2001 Mean flow and turbulence structure of open-channel flow through non-emergent vegetation. *J. Hydr. Engng* **127**, 392–402.

Manes, C., Pokrajac, D. & McEwan, I. 2007 Double-averaged open-channel flows with small relative submergence. *J. Hydr. Engng* **133**, 896–904.

Mignot, E., Bartheleemy, E. & Hurther, D. 2009 Double-averaging analysis and local flow characterization of near-bed turbulence in gravel-bed channel flows. *J. Fluid Mech.* **618**, 279–303.

Nikora, V., Goring, D., McEwan, I. & Griffiths, G. 2001 Spatially averaged open-channel flow over rough bed. *J. Hydr. Engng* **127**, 123–133.

Nikora, V., Koll, K., McEwan, I., McLean, S. & Dittrich, A. 2004 Velocity distribution in the roughness layer of rough-bed flows. *J. Hydr. Engng* **130**, 1036–1042.

Nikora, V., McEwan, I., McLean, S., Coleman, S., Pokrajac, D. & Walters, R. 2007 Double-averaging concept for rough-bed open-channel and overland flows: theoretical background. *J. Hydr. Engng* **133**, 873–883.

Orlandi, P. & Leonardi, S. 2008 Direct numerical simulation of three-dimensional turbulent rough channels: parameterization and flow physics. *J. Fluid Mech.* **606**, 399–415.

Raupach, M. R., Antonia, R. A. & Rajagopalan, S. 1991 Rough-wall boundary layers. *Appl. Mech. Rev.* **44**, 1–25.

Raupach, M. R. & Shaw, R. H. 1982 Averaging procedures for flow within vegetation canopies. *Bound.-Lay. Meteorol.* **22**, 79–90.

Schultz, M. P. & Flack, K. A. 2013 Reynolds-number scaling of turbulent channel flow. *Phys. Fluids* **25**, 025104–1—13.

Scotti, A. 2006 Direct numerical simulation of turbulent channel flows with boundary roughened with virtual sandpaper. *Phys. Fluids* **18**, 031701–1—4.

Yuan, J. & Piomelli, U. 2014 Numerical simulations of sink-flow boundary layers over rough surfaces. *Phys. Fluids* **26**, 015113–1—015113–28.